

Cosmography with Λ -Szekeres Models

Morag Hills^a and Asta Heinesen^b

^aSchool of Physical & Chemical Sciences, University of Canterbury, Private Bag 4800, Christchurch 8140, New Zealand

^bDepartment of Physics and Astronomy, Queen Mary University of London, UK

^bNiels Bohr Institute, Blegdamsvej 17, DK-2100 Copenhagen, Denmark

E-mail: morag.hills@pg.canterbury.ac.nz, asta.heinesen@nbi.ku.dk

Abstract. The cosmological tensions present in the Λ cold dark matter model that have emerged and strengthened over recent years motivate model independent approaches to analysing data. Cosmography is useful for interpreting data in cosmology without imposing assumptions about the field equations of gravity or the matter content in the Universe. Some cosmography methods, denoted *covariant cosmography*, go even further and stay agnostic to the underlying space-time metric. Due to their high level of generality, covariant cosmography methods can incorporate the anisotropies and inhomogeneities in the observer's vicinity, and may in turn inform about the associated curvature of the relevant structures in our cosmic neighbourhood. Thus, covariant cosmography is a powerful model-independent tool for analysing cosmological data while also enabling the mapping of our local cosmic neighbourhood. In order to be able to explore the covariant cosmography framework to its fullest, it must be tested in tractable models and simulations. In this paper we derive the cosmography of luminosity distance to fourth order in redshift and investigate it in the special case of axially symmetric Szekeres models. We compare the numerical results for the distance-redshift relations of synthetic observers placed within the Szekeres structures with the predictions from the cosmography, and comment on the found level of approximation of the cosmography in relation to other results in the litterature.

Contents

1	Introduction	1
2	Covariant Cosmography Formalism	3
2.1	Fundamental congruences	3
2.2	Distance-redshift measures	4
2.3	Alternative approximants	6
3	Szekeres cosmological models	7
3.1	Line element and field equations	7
3.2	Model parameterisation	9
4	Ray tracing methodology	10
4.1	Null geodesic equations	10
4.2	Ray initialisation	12
5	Results	13
5.1	Directional variation of the cosmographic parameters	13
5.2	Comparison of ray traced and cosmographic luminosity-distances	14
5.3	Assessment of Padé Approximants	18
6	Discussion and conclusion	20
A	Numerical Convergence & Accuracy	21
B	Null vector initialisation procedure	22
C	Evolution of the direction vector of the photon congruence	23
D	Metric Derived Quantities	23
D.1	Non-Zero Christoffel Symbols	24
D.2	Non-Zero Components of the Ricci Tensor	24
D.3	Derivatives of the Szekeres dipole function	25

1 Introduction

Cosmography is a route for achieving constraints on the expansion and curvature of the Universe without the specification of the field equations of gravity or the matter content of the space-time [1–3]. The methods of cosmography thus offer a truly model independent framework of analysing data that is complementary to parametrized methods that specify the dynamical model of the space-time in order to extract information about the space-time within that model scenario. Cosmography is useful for testing the consistency

of the Λ cold dark matter (Λ CDM) cosmology, and is flexible enough to include virtually any extension of it.

With the still increasing list of possible theoretical scenarios for accounting for the cosmic tensions faced in the Λ CDM model, ranging from modified gravity scenarios to the addition of extra matter fields, cosmography presents an appealing framework for testing the extensions of the baseline Λ CDM model in a model-independent setup that can include a very diverse set of physical scenarios in the same setup.

Cosmography has mainly been used for the purpose of constraining kinematic variables within the Friedmann-Lemaître-Robertson-Walker (FLRW) class of metrics, cf., e.g., [3]. However, cosmography is not limited to the FLRW geometries, and the methods of cosmography can in fact be extended in a, perhaps surprisingly, straightforward way to arbitrary space-time metrics; see [2, 4] for early work on such extensions. Thus, cosmography can be used to extract model-independent information about the (anisotropic and inhomogeneous) degrees of freedom of the space-time geometry, with methods for this presented in [5–8]. A number of recent papers have demonstrated the feasibility of this aim within numerical relativity simulations [9–11], and have also taken the first steps to analyze real data [12–15].

Cosmography has been most widely investigated for measurements of luminosity distance and angular diameter distance, but can in principle be carried out for any observation that has a geometrical prediction, for instance position drift (once measured by *Gaia*) [16] and redshift drift (measurable in the future by the Extremely Large Telescope and the Square Kilometre Array) [17–19]. In this work we focus on the cosmography for luminosity distance, but note that the drift effects are interesting complementary observables to consider for distinguishing different cosmological scenarios [20].

One of the main challenges in applying cosmography to data is to control the level of approximation of the (truncated) cosmography and its convergence to the underlying distance-redshift relation. While the convergence properties of the FLRW cosmographic series for cosmic distances are reasonably well understood [21–23], little work has been done in the literature for testing the convergence/level of approximation of space-times with anisotropies and/or inhomogeneities. An exception is the recently published work [24, 25] in which analyses of the accuracy of the cosmographic approach within Lemaître-Tolman-Bondi (LTB) models were carried out. The LTB models are spherically-symmetric, and while they present good idealized models of isolated voids in the Universe, they are not ideal for describing large-scale over-densities of galaxies that are typically elongated in shape.

The Szekeres cosmological models are the most general exact solutions obtained for space-times sourced by dust. They are irrotational silent models universe models of Petrov type D, and they do not possess globally-defined Killing vectors. They thus present flexible models that may describe wall-like structures that are known to exist in the observed cosmic web of galaxies. Szekeres cosmological models are thus interesting tractable solutions of observational interest. The Hubble diagram has been investigated in a few studies employing ray tracing in Szekeres solutions, such as in [26]. As far as we are aware, no paper has yet conveyed a detailed study of cosmography and convergence

properties for Szekeres solutions, although a recent paper takes the first steps towards such investigations [27].

In this paper, we investigate the luminosity-distance cosmography for Szekeres space-times, with the purpose of systematically examining the approximation of the theoretical cosmography expressions relative to the exact luminosity distances computed by ray-tracing. In section 2, we review the general cosmographic expressions for luminosity distance derived previously, and we extend these results to include the fourth order term in the cosmographic series. In section 3, we review the Szekeres cosmological models for which we investigate cosmography in this paper. In section 4, we explain the ray tracing algorithm for calculating exact distances and redshifts in our codes. In section 5 we present and our results. We finally discuss our results in the context of recent work in the literature and conclude on our analysis in section 6.

Notation and conventions:

We use units where $c = 1$ and $G = 1$, where c is the speed of light and G is the gravitational constant. Greek letters μ, ν, \dots are used for space-time indices in a general coordinate system. The signature of the space-time metric $g_{\mu\nu}$ is $(- + ++)$ and the covariant derivative ∇_μ is the usual metric-preserving Levi-Civita connection. Vectors, V^μ , are sometimes written in the basis free notation \mathbf{V} for the sake of compactness. Covariant derivatives of vectors are occasionally written as $V^\mu_{;\nu} \equiv \nabla_\nu V^\mu$.

2 Covariant Cosmography Formalism

2.1 Fundamental congruences

We shall now formulate a *covariant luminosity distance cosmography*, i.e., a Taylor series expansion of luminosity distance in redshift, valid in any Lorentzian space-time where light is travelling on non-caustic null geodesics and where the observers and emitters (of light and gravitational waves) of interest are collectively described by a time-like congruence of worldlines. The derivations follow those of [7], and the reader is referred to this paper for details.

There are two congruences of interest to be considered in obtaining the generalised luminosity distance Hubble law. The first of these congruences is the time-like congruence, belonging to the reference observers and emitters, which is described by the tangent vector field \mathbf{u} - the 4-velocity of the observers and emitters. The second of these congruences is the light-cone forming irrotational¹ geodesic congruence of photons, described by the affinely parametrised tangent null vector \mathbf{k} . This vector corresponds to the 4-momentum of the photons emitted and observed between the members of the time-like observer-emitter congruence.

The photon 4-momentum \mathbf{k} can be decomposed into parallel and orthogonal parts to the 4-velocity \mathbf{u} as follows:

$$k^\mu = E(u^\mu - e^\mu), \quad E \equiv -k^\mu u_\mu, \quad (2.1)$$

¹The irrotational property follows directly from the requirement that the congruence represents the lightcone of an observer.

where the unit vector field \mathbf{e} is orthogonal to \mathbf{u} , and indicates the spatial propagation direction of a photon measured by the observers comoving with \mathbf{u} . As such, one can consider \mathbf{e} as a radial unit vector when evaluated at the vertex of the observer's lightcone. The function E is the energy of the photon congruence inferred by the observers comoving with \mathbf{u} , and can be fixed through the freedom in rescaling of the affine parametrisation of \mathbf{k} [28].

The evolution of the energy function E along the null geodesics can be formulated in terms of projected dynamical variables of \mathbf{u} in the following way:

$$\frac{dE}{d\lambda} = -k^\mu \nabla_\mu (k^\nu u_\nu) = -E^2 \mathfrak{H}, \quad (2.2)$$

where we have defined the derivative along the photon 4-momentum $\frac{d}{d\lambda} \equiv k^\mu \partial_\mu$. By taking the covariant derivative of E with respect to the affine parameter λ along the geodesics, we obtain the parameter

$$\mathfrak{H} \equiv \frac{1}{3} \Theta - e^\mu a_\mu + e^\mu e^\nu \sigma_{\mu\nu}, \quad (2.3)$$

which is a truncated multipole series in the spatial unit vector \mathbf{e} , wherein Θ is the volume expansion rate of the congruence, $\sigma_{\mu\nu}$ is the volume shear rate describing its symmetric anisotropic deformation, and $a^\mu = u^\mu \nabla_\nu u^\nu$ is the 4-acceleration of the field. The coefficients of (2.3) are expressed in terms of the kinematic decomposition of the matter frame as

$$\begin{aligned} \nabla_\nu u_\mu &= \frac{1}{3} \Theta h_{\mu\nu} + \sigma_{\mu\nu} + \omega_{\mu\nu} - a_\mu u_\nu, \\ \Theta &\equiv \nabla_\mu u^\mu, \quad \sigma_{\mu\nu} \equiv h_{(\mu}^\beta h_{\nu)}^\alpha \nabla_\alpha u_\beta - \frac{1}{3} \Theta h_{\mu\nu}, \quad \omega_{\mu\nu} \equiv h_{[\mu}^\beta h_{\nu]}^\alpha \nabla_\alpha u_\beta, \end{aligned} \quad (2.4)$$

where $\omega_{\mu\nu}$ describes the rotational deformation of the congruence and $h_{\mu\nu} = g_{\mu\nu} + u_\mu u_\nu$ is the projection tensor to the matter frame, with round parentheses implying symmetrisation over the selected indices and square brackets implying anti-symmetrisation.

The function \mathfrak{H} , as given by (2.3), which we denote the *effective Hubble parameter* describes the rate of change of photon energies with affine distance in general spacetimes, and thus generalise the isotropic Hubble parameter H in FLRW spacetime. In the following section 2.2, we shall see that \mathfrak{H} indeed defines the leading order distance-redshift proportionality law in the general spacetime setting, thus generalizing the wellknown Hubble law. We will also demonstrate how we can further obtain the equivalent *effective cosmographic parameters* for the FLRW deceleration q , jerk j and snap s parameters, by taking successively higher order derivatives of (2.3) and (2.4).

2.2 Distance-redshift measures

The angular diameter distance d_A of an observed source, which measures the physical extent of an object relative to its angular extent subtended on the observer's sky, is given by

$$d_A = \sqrt{\frac{\delta A}{\delta \Omega}}, \quad (2.5)$$

where δA is the cross-sectional area of the source (perpendicular to the 4-velocity \mathbf{u} and 4-momentum \mathbf{k} of the source congruence) and $\delta\Omega$ is the observed angular extent. As the light bundle propagates through space, the angular diameter distance will evolve according to the expansion rate of the null congruence, $\hat{\theta} = \nabla_\mu k^\mu$, as follows

$$\frac{dd_A}{d\lambda} = \frac{1}{2}\hat{\theta}d_A. \quad (2.6)$$

It follows from the Sachs equations, defining the deformation rates of the expansion $\hat{\theta}$ and shear $\hat{\sigma}_{\mu\nu}$ of the null congruence, that

$$\frac{d\hat{\theta}}{d\lambda} = -\frac{1}{2}\hat{\theta}^2 - \hat{\sigma}_{\mu\nu}\hat{\sigma}^{\mu\nu} - k^\mu k^\nu R_{\mu\nu}, \quad (2.7a)$$

$$\frac{D\hat{\sigma}_{\mu\nu}}{d\lambda} = -\hat{\theta}\hat{\sigma}_{\mu\nu} - p_\mu^\gamma p_\nu^\sigma k^\alpha k^\beta C_{\gamma\alpha\sigma\beta}, \quad (2.7b)$$

where we have defined the covariant derivative along the photon 4-momentum $\frac{D}{d\lambda} \equiv k^\mu \nabla_\mu$, and where $C_{\gamma\alpha\sigma\beta}$ is the Weyl curvature tensor of the space-time. We can express the second derivative of the angular diameter distance as

$$\frac{d^2 d_A}{d\lambda^2} = -\left(\hat{\sigma}^2 + \frac{1}{2}k^\mu k^\nu R_{\mu\nu}\right)d_A \quad (2.8)$$

by substituting (2.7a) into the derivative of (2.6). In the above, $p_{\mu\nu} = g_{\mu\nu} + u_\mu u_\nu - e_\mu e_\nu$ is the projection tensor onto the 2-dimensional *screen spaces* that are orthogonal to u^μ and e^μ . The first term of (2.8), containing the scalar shear, $\hat{\sigma}^2 \equiv \frac{1}{2}\hat{\sigma}^{\mu\nu}\hat{\sigma}_{\mu\nu}$, of the null congruence is responsible for Weyl focusing of the congruence, whereas the second term is responsible for Ricci focusing of the congruence.

The luminosity distance, d_L , to a source is defined in terms of the source's bolometric luminosity L at the source and measured bolometric flux F by the observer:

$$d_L = \sqrt{\frac{L}{4\pi F}}. \quad (2.9)$$

One can relate the angular diameter distance to the luminosity distance d_L separating the source and observer through Etherington's reciprocity theorem, assuming that photon conservation holds, as

$$d_L = (1+z)^2 d_A, \quad (2.10)$$

where the redshift is defined as

$$z \equiv \frac{E}{E_o} - 1, \quad (2.11)$$

where E_o is the energy of the photon as measured by the observer at the vertex of the past lightcone.

Using the known expressions for the derivatives of E and d_A with respect to λ derived in the above equations (2.2), (2.6), and (2.8), and together with the definition of redshift in (2.11), we can write the Taylor series expansion of d_L in z [see 7, for details]

$$d_L(z) = d_L^{(1)}z + d_L^{(2)}z^2 + d_L^{(3)}z^3 + \mathcal{O}(z^4), \quad (2.12)$$

wherein the coefficients may be expressed in terms the effective cosmographic parameters evaluated at the vertex point of the congruence, i.e., at the point of observation as denoted by o subscripts, as follows:

$$d_L^{(1)} = \frac{1}{\mathfrak{H}_o}, \quad (2.13a)$$

$$d_L^{(2)} = \frac{1 - \mathfrak{Q}_o}{2\mathfrak{H}_o}, \quad (2.13b)$$

$$d_L^{(3)} = \frac{-1 + 3\mathfrak{Q}_o^2 + \mathfrak{Q}_o - \mathfrak{J}_o + \mathfrak{R}_o}{6\mathfrak{H}_o}, \quad (2.13c)$$

$$d_L^{(4)} = \frac{2 - 2\mathfrak{Q}_o - 15\mathfrak{Q}_o^2 - 15\mathfrak{Q}_o^3 + 5\mathfrak{J}_o + 10\mathfrak{Q}_o\mathfrak{J}_o + \mathfrak{S}_o - 2\mathfrak{R}_o(1 + 3\mathfrak{Q}_o)}{24\mathfrak{H}_o} \quad (2.13d)$$

with

$$\mathfrak{Q} \equiv -1 - \frac{1}{E} \frac{\frac{d\mathfrak{H}}{d\lambda}}{\mathfrak{H}^2}, \quad (2.14a)$$

$$\mathfrak{R} \equiv 1 + \mathfrak{Q} - \frac{1}{2E^2} \frac{k^\mu k^\nu R_{\mu\nu}}{\mathfrak{H}^2}, \quad (2.14b)$$

$$\mathfrak{J} \equiv \frac{1}{E^2} \frac{\frac{d^2\mathfrak{H}}{d\lambda^2}}{\mathfrak{H}^3} - 4\mathfrak{Q} - 3, \quad (2.14c)$$

$$\mathfrak{S} = \frac{1}{E^3} \frac{\frac{d^3\mathfrak{H}}{d\lambda^3}}{\mathfrak{H}^4} + \frac{1}{E^3} \frac{\frac{d}{d\lambda}(k^\mu k^\nu R_{\mu\nu})}{\mathfrak{H}^3} - 8\mathfrak{R} + 4\mathfrak{Q}^2 + 35\mathfrak{Q} + 9\mathfrak{J} + 23. \quad (2.14d)$$

Immediately, we find the coefficients in (2.13) to be analogous to the typical presentation of the FLRW series expansion coefficients: $d_L^{(1)} = \frac{1}{H_o}$, $d_L^{(2)} = \frac{1-q_o}{2H_o}$, $d_L^{(3)} = \frac{-1+3q_o^2+q_o-j_o+\Omega_k}{6H_o}$, and $d_L^{(4)} = \frac{2-2q_o-15q_o^2(1+q_o)+5j_o+10q_oj_o+s_o-2\Omega_k(1+3q_o)}{24H_o}$, where Ω_k is the FLRW spatial curvature density. We thus identify the parameters in (2.14) as *effective cosmographic parameters*, in addition to the previously identified effective Hubble parameter \mathfrak{H} defined by (2.3): the effective ‘deceleration’ (2.14a), ‘curvature’ (2.14b), ‘jerk’ (2.14c) and ‘snap’ (2.14d) parameters, respectively. The 3rd order expansion agrees with that already derived in [7], and our results extend the work of [7] with the added 4th order term. Kalbouneh *et al.* [29] have previously calculated the 4th order cosmographic series using a slightly different version of the formalism presented in this paper. We have compared our results to theirs, with agreement up to third order.

Computing the effective cosmographic parameters in (2.14) requires taking appropriate covariant derivatives (with respect to λ) of \mathfrak{H} (2.3). To investigate the 4th order cosmography, we thus computed all covariant derivatives up to 3rd order of the variables Θ , $\sigma_{\mu\nu}$ and e^μ entering in \mathfrak{H} (2.3). Additionally, for (2.14d), we computed the 1st order covariant derivative of $R_{\mu\nu}$. For convenience, we provide expressions for the derivatives of e^μ up to 3rd in appendix C.

2.3 Alternative approximants

The cosmographic Taylor series expansion in powers of redshift typically converge for $z \leq 1$ [30], at least when one considers the standard isotropic cosmographic expansion

of the Friedmann solutions. Various solutions have been proposed to extend the convergence radius of the standard cosmographic series expansion for d_L and d_A above $z = 1$, including parameterisations by auxiliary variables, Chebyshev polynomials and Padé approximants (e.g. [22, 23, 30–34]) – each with their own benefits and shortcomings. Padé approximants can also help increase the convergence radii for cosmographies performed within realistic anisotropic space-times [35]. However, these approximants are yet to be fully explored in the context of inhomogeneous models. In this paper, we consider a range of appropriate Padé approximants [36, 37] as alternatives to the standard Taylor series expansion for d_L (2.12). Given a Taylor series expansion of the form

$$f(x) = \sum_{k=0}^K c_k x^k, \quad (2.15)$$

for a function $f(x)$, the corresponding Padé approximant $P(x)$ of order $[M/N]$ is the rational polynomial

$$P(x)_{M/N} = \frac{\sum_{i=0}^M a_i x^i}{1 + \sum_{j=1}^N b_j x^j}, \quad (2.16)$$

where M and N give the orders of the numerator and denominator, respectively, and $M + N \leq K$. Furthermore, through setting each order of (2.15) and (2.16) equal to each other, one can solve for the coefficients a_i and b_j within (2.16) using the known coefficients c_k of the Taylor series.

3 Szekeres cosmological models

3.1 Line element and field equations

The class of Szekeres models considered in this paper contain only a pressureless, irrotational dust source with rest-mass density ρ and cosmological constant Λ , with the metric defined in synchronous comoving coordinates. The Szekeres line element in its ‘projective coordinate’ (p, q) representation is

$$ds^2 = -dt^2 + \frac{(R' - R \mathcal{E}'/\mathcal{E})^2}{\epsilon - k} dr^2 + \frac{R^2}{\mathcal{E}^2} (dp^2 + dq^2), \quad (3.1)$$

where primes denote a partial derivative with respect to the radial coordinate, r . Note that r does not correspond to the radial distance from the origin of the model, as it otherwise does in the LTB models, because the non-concentric arrangement of Szekeres shells means that each shell’s origin need not coincide. The parameter $\epsilon = +1, 0, -1$ delineates between the quasi-spherical, quasi-planar and quasi-pseudo-spherical subtypes; we consider the well-studied $\epsilon = +1$ case here. The function $R = R(t, r)$ is the proper area radius of a given shell, and $k = k(r)$ is the local spatial curvature parameter.

The function $\mathcal{E} = \mathcal{E}(r, p, q)$ in Szekeres metric (3.1) describes the deviation of a given Szekeres model from its corresponding LTB model limit, and reads

$$\mathcal{E}(r, p, q) = \frac{(p - P(r))^2 + (q - Q(r))^2 + \epsilon S(r)}{2S(r)}, \quad (3.2)$$

where the dipole functions $S(r)$, $P(r)$ and $Q(r)$ characterise the dipole asymmetry. In appendix D, we provide the non-zero Chrisoffel symbols and Ricci tensor components of the Szekeres models in projective coordinates, as well as the derivatives of \mathcal{E} which enter the Ricci tensor (see also [27] for useful curvature identities).

The Einstein equations of the Szekeres model are

$$R_{\mu\nu} = 8\pi \left(T_{\mu\nu} - \frac{1}{2} T g_{\mu\nu} \right) - \Lambda g_{\mu\nu} = 8\pi \rho \left(u_\mu u_\nu + \frac{1}{2} g_{\mu\nu} \right) - \Lambda g_{\mu\nu}, \quad (3.3)$$

where ρ is the rest-mass density of the source dust. They reduce to two independent equations, the first being the time evolution of $R(t, r)$,

$$\dot{R}(t, r)^2 = \frac{2M(r)}{R(t, r)} - k(r) + \frac{1}{3}\Lambda R(t, r)^2, \quad (3.4)$$

where the function $M(r)$ is the active gravitational mass contained within a constant- r shell in the quasi-spherical case, which is responsible for generating the gravitational field². Integrating (3.4), we further obtain

$$t - t_B(r) = \int_0^{R(t, r)} \left(\frac{2M(r)}{\tilde{R}} - k(r) + \frac{1}{3}\Lambda \tilde{R}^2 \right)^{-1/2} d\tilde{R}, \quad (3.5)$$

where $t_B(r)$ is the ‘bang-time’ at a given r ³. The second equation we obtain from the Einstein equations is the mass density equation

$$4\pi\rho(t, r, p, q) = \frac{M' - 3M\mathcal{E}'/\mathcal{E}}{R^2(R' - R\mathcal{E}'/\mathcal{E})}, \quad (3.6)$$

where the coordinate dependence of the right hand side of the equation is implicit for the sake of compactness. It is evident here that the factors of \mathcal{E}'/\mathcal{E} control the dipole distribution of matter. The Szekeres line element (3.1) can be recast in spherical coordinates

²This is distinct from the integrated mass of all dust particles comprising the matter content of the model [38].

³The radially dependent bang-time function $t_B(r)$ describes the time at which a given constant- r Szekeres shell emerges from the $R(t_B, r) = 0$ singularity, as each shell evolves independently of each other.

via a Riemannian stereographic projection

$$\begin{aligned}
ds^2 = & -dt^2 + \frac{1}{1-k} \left[R' - \frac{R}{S} (S' \cos \theta + \mathcal{N} \sin \theta) \right]^2 dr^2 \\
& + \left[\frac{S' \sin \theta + \mathcal{N} (1 - \cos \theta)}{S} \right]^2 R^2 d\theta^2 + \left[\frac{(\partial_\phi \mathcal{N})(1 - \cos \theta)}{S} \right]^2 R^2 d\phi^2 \\
& - 2 \frac{S' \cos \theta + \mathcal{N} \sin \theta}{S} R^2 dr d\theta + 2 \frac{(\partial_\phi \mathcal{N})(1 - \cos \theta)}{S} R^2 \sin \theta dr d\phi \\
& + R^2 (d\theta^2 + \sin^2 \theta d\phi^2)
\end{aligned} \tag{3.7}$$

where $\mathcal{N}(r, \phi) = (P' \cos \phi + Q' \sin \phi)$. As the Szekeres models we examine in this paper are axially symmetric, we restrict $S'(r)$ to be the only non-zero dipole function, so that $\mathcal{N}(r, \phi) = 0$. The models are thus symmetric about the axis defined by $S(r)$ with the dipole position only varying in the θ coordinate, as there will be no ϕ dependence in \mathcal{E}'/\mathcal{E} when $P' = Q' = 0$.

The projective coordinate representation of the metric (3.1) is straight-forward to use in deriving various products of the metric, owing largely to its diagonalised form. However, for the purpose of our specific numerical ray tracing scheme that we employ in this paper, the spherical coordinates of (3.7) are convenient and avoid coordinate singularities along the symmetry axis [39]. Thus, in the present work, we use the spherical coordinate form of the Szekeres metric for ray tracing, while we use the simpler projective coordinates for the computation of the covariant cosmographic parameters in (2.14).

3.2 Model parameterisation

We define the background FLRW model that our Szekeres models approach at large radii by setting the cosmological parameters to the *Planck* parameter estimates [40],

$$(\Omega_{m0}, \Omega_{\Lambda0}, \Omega_{k0}, h) = (0.315, 0.685, 0.0, 0.673), \tag{3.8}$$

where Ω_{m0} , $\Omega_{\Lambda0}$ and Ω_{k0} are the present-time Friedmann values of the matter, cosmological constant and spatial curvature densities, respectively. Within our simulations, the big-bang singularity is made simultaneous for all comoving observers through fixing $t_B(r) = 0$ for all r in (3.5). We determine the present age of the universe via the following analytic solution of the background Friedmann equation

$$t_0 = \frac{1}{3H_0\sqrt{\Omega_{\Lambda0}}} \ln \left(\frac{1 + \sqrt{\Omega_{\Lambda0}}}{1 - \sqrt{\Omega_{\Lambda0}}} \right), \tag{3.9}$$

as we have $\Omega_{k0} = 0$ for our flat FLRW background model. The function $R(t, r)$ is set to coincide with the coordinate- r at the present time t_0 , such that $R(t_0, r) = r$, which is used as the initial condition for (3.4).

In the axially symmetric Szekeres models that we investigate, the dipole functions are defined as,

$$P(r) = 0, \quad Q(r) = 0, \quad S(r) = \left(\frac{r}{1 \text{ Mpc}} \right)^\alpha \text{ Mpc}, \tag{3.10}$$

where the parameter α is introduced to effectively control the strength of the dipole in the density distribution.

	α	δ_0	Δr
Model 1	0.5	-0.8	$40 h^{-1} \text{ Mpc}$
Model 2	0.5	-0.8	$80 h^{-1} \text{ Mpc}$

Table 1. Parameter values for model 1 and model 2. These parameters are used within (3.13) to control the behaviour of the Szekeres mass profile (3.11).

We parametrise the mass distribution of the Szekeres solution as follows

$$M(r) = M_0(r) + \delta M(r) \quad (3.11)$$

where the homogeneous mass profile $M_0(r)$ of the FLRW background and the deviation of the mass profile from the background $\delta M(r)$ are respectively given by

$$M_0(r) = \frac{4}{3}\pi\bar{\rho}(t_0)r^3 = \frac{1}{2}\Omega_{m0}H_0^2r^3, \quad \delta M(r) = \frac{1}{2}\Omega_{m0}H_0^2r^3\delta(r). \quad (3.12)$$

We finally construct our Szekeres models by specifying their density profiles (3.6) through the function $\delta(r)$ entering in equation (3.12). We select the following form:

$$\delta(r) = \delta_0 \exp\left[-\left(\frac{r}{2\Delta r}\right)^2\right], \quad (3.13)$$

wherein the parameters δ_0 and Δr allow one to tune the characteristics of the resulting density profile. Setting the local perturbation parameter $\delta_0 \in [-1, 0)$ produces an under-density or void centred at the origin $r = 0$. The parameter Δr is used to control the steepness of the void density profile, i.e., the transition rate between the under-dense and over-dense regions of the model. The profile (3.13) thus allows us to describe a local under density (with a corresponding over density) at varying characteristic radii. We summarise the models and observer positions that we investigate in our analysis in tables 1 and 2. The density profiles for the models in table 1 are shown in fig. 1 for selected directions away from the centre of the under density.

4 Ray tracing methodology

4.1 Null geodesic equations

Performing a thorough analysis of the covariant cosmographic expansions requires one to compute the exact quantities of interest, e.g. the redshift and angular diameter distance,

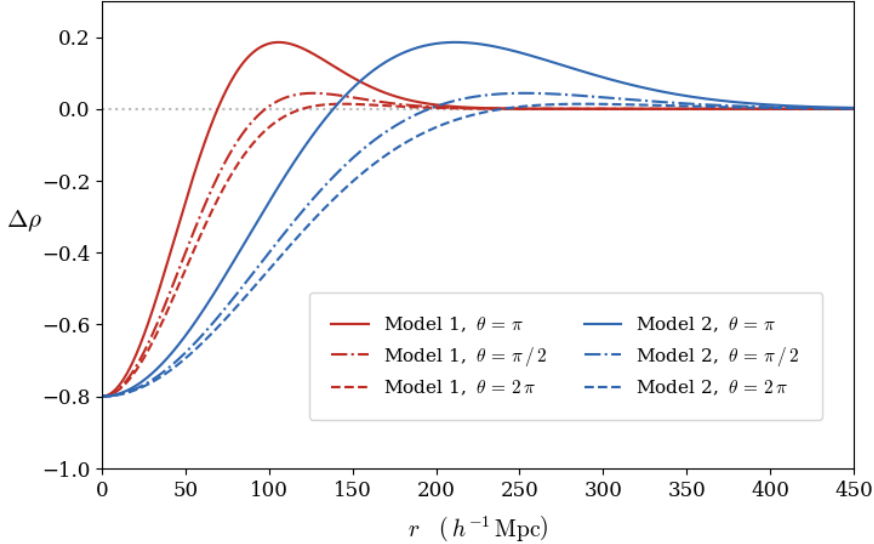


Figure 1. The initial present time 2D density profiles of model 1 and model 2, normalised to the background FLRW density $\Delta\rho = (\rho - \bar{\rho})/\bar{\rho}$. These profiles are plotted from the coordinate centre of the Szekeres model, with r being the radial distance from the coordinate centre. In terms of the angular Szekeres coordinate θ , solid $\theta = \pi$ lines corresponding to the angular position of the maximum over-density magnitude, while dashed $\theta = 2\pi$ lines correspond to the angular position of the minimum over-density magnitude. Dash-dotted lines give the over-density magnitude located 90° from these extrema. The parameter values of each profile are given in table 1.

as seen by a given fiducial observer within our Szekeres models for comparative means. Ray tracing analyses in both Szekeres and LTB models have been performed for various purposes in past research (see, e.g. [10, 41, 42]). In this paper, we adopt a similar ray tracing scheme to that used in [41], and later developed in [43, 44]. This scheme is centred around the numerical integration of the null geodesic equations,

$$k^\mu \nabla_\mu k^\gamma = \frac{dk^\gamma}{d\lambda} + \Gamma^\gamma_{\mu\nu} k^\mu k^\nu = 0, \quad (4.1)$$

where $\Gamma^\gamma_{\mu\nu}$ are the Christoffel symbols and λ is the affine parameter along the light ray and the tangent null vectors k^μ are defined as

$$k^\mu = \frac{dx^\mu}{d\lambda}. \quad (4.2)$$

Due to the complexity of the spherical coordinate representation of the Szekeres metric, we do not include their precise forms in this paper. However, the non-zero Christoffel symbols in projective coordinates are presented for reference in appendix D.1 for completeness. The primary aim of our ray tracing procedure is to obtain a given observable quantity, such as the luminosity distance d_L or angular diameter distance d_A , as observed at a fixed target redshift z or vice versa, by backwards propagating the null geodesic equations through spacetime until the target is achieved.

For the numerical ray tracing simulations undertaken in this investigation, we use the HEALPix (Hierarchical Equal Area isoLatitude Pixelisation) scheme via the PYTHON and JULIA implementations `healpy` [45] and `healpix.jl` [46], respectively. We numerically solve the system of ODEs for the null geodesic equations (4.1) using the `tsit5()` method provided by the `DifferentialEquations.jl` package [47], which is an implementation of Tsitouras' 5th order explicit Runge-Kutta method [48].

For each pixel on the observer's HEALPix sky, we *backwards propagate* a light ray until the redshift z is achieved, and then evaluate the luminosity distance at the corresponding event. We note that in our description of the ray tracing method that follows, we define our null vectors $k_{\text{obs}}^{\hat{\alpha}}$ at the observer to be future-pointing. However, our codes are constructed using past-pointing null vectors, which is simply a choice of convention. For further technical details regarding the stability and convergence of the numerical implementation; see appendix A.

4.2 Ray initialisation

In order to determine the redshift z of the source, we propagate rays in from the observer to the source by effectively tracking the solutions of eight ODEs, corresponding to (4.1) and (4.2) in the variables $k^\mu = (k^t, k^r, k^\theta, k^\phi)$ and the ray position vector $x^\mu = (x^t, x^r, x^\theta, x^\phi)$ at each step of the numerical integration routine. At the observer, we initialise $k^t = 1$ via our choice of affine parameter so that the redshift is given by

$$1 + z = \frac{(k^\mu u_\mu)_{\text{src}}}{(k^\mu u_\mu)_{\text{obs}}} = \frac{k_{\text{src}}^t}{k_{\text{obs}}^t} = k_{\text{src}}^t, \quad (4.3)$$

where we note that for the comoving (geodesic) Szekeres observer we simply have $u_\mu = (-1, 0, 0, 0)$. From the decomposition (2.1) of the null vector k^μ , the spatial unit vector $e^{\hat{\alpha}} = (0, \hat{\mathbf{n}})$ is equivalent to the direction on the observer's sky in which a source is observed. The direction vector can be converted in terms of equatorial coordinates (ℓ, b) on the sky, (or as in our numerical implementation, as individual indexed pixels on a HEALpix map). By then numerically determining k_{src}^t through (backwards) propagation of the ray from observer to source, via integration of the null geodesic equations (4.1) that one may obtain the source's z in a given Szekeres model.

The angular diameter distance is computed via the focusing equation (2.8). We set the Weyl focusing term $\propto \hat{\sigma}^2$ to zero in this analysis⁴, under the assumption that it is subdominant. (See, e.g., [41, 49] for a justification of this.) Under this approximation, the focusing equation (2.8) becomes

$$\frac{d^2 d_A}{d\lambda^2} + 4\pi\rho (k^t)^2 d_A = 0, \quad (4.4)$$

which follows from the Einstein equations (3.3). Lastly, it remains in the initialisation procedure to set up the initial null vector of each ray in the local orthonormal frame. For each angular direction of observation (ℓ, b) at the observer, where in this case b is the

⁴For full numerical solutions including the Weyl term, see, e.g. [10, 24]

co-latitude and ℓ the longitude measured in radians, we first determine the Cartesian direction vector $\hat{\mathbf{n}}$ in the local inertial frame

$$\hat{n}^x = \cos b \cos \ell, \quad \hat{n}^y = \cos b \sin \ell, \quad \hat{n}^z = \sin b, \quad (4.5)$$

such that the initial null vector is then given by $k_{\text{obs}}^{\hat{\alpha}} = (1, -\hat{\mathbf{n}})$ in this choice of coordinates. We initialise our ray null vectors in the Szekeres spherical coordinates of (3.7) by contracting the local orthonormal basis tetrad $e^{\mu}_{\hat{\alpha}}$ with $k^{\hat{\alpha}}$ at the observer position, so that in these coordinates: $k_{\text{obs}}^{\mu} = e^{\mu}_{\hat{\alpha}} k^{\hat{\alpha}}|_{\text{obs}}$. The details of this normalisation procedure are described in further detail in appendix B.

5 Results

5.1 Directional variation of the cosmographic parameters

The covariant cosmographic parameters (2.14) are constructed at the observer location via the kinematical variables of the observer congruence (2.4), their covariant derivatives, and the spatial direction of observation on the observer's sky. The sky variation of these parameters is shown in fig. 2 for observer 1 (see table 2) in model 1 (see table 1). In

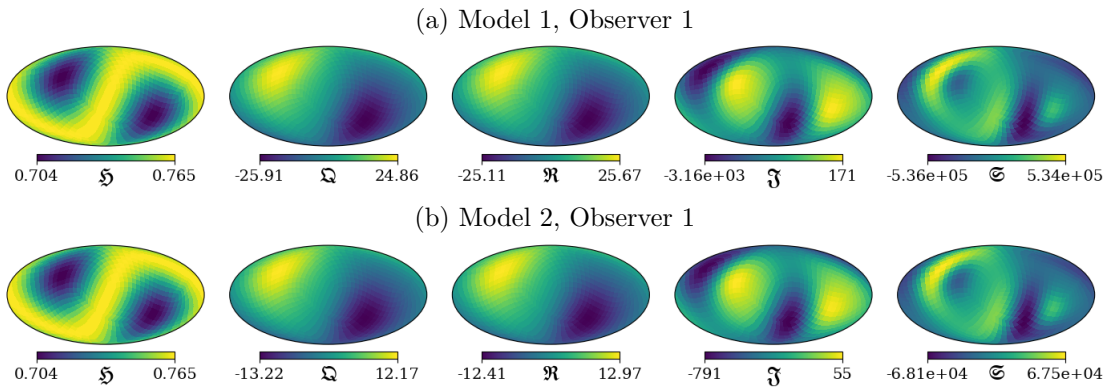


Figure 2. Variation of the covariant cosmographic parameters (2.3) and (2.14) for observer 1 in model 1 and model 2.

fig. 2, we observe that there is a clear quadrupolar distribution of \mathfrak{H} which is caused by the shear tensor of the observer congruence. We also observe a clear dipolar distribution in the generalised deceleration parameter \mathfrak{Q} , agreeing with the stated expectations of [9]. While not visually apparent in the figure, the distribution of \mathfrak{Q} also contains small monopole and octupole contributions, as expected. The dominant dipole in \mathfrak{Q} can be attributed to terms involving $k^{\mu} \nabla_{\mu} \Theta$, and this dipole is therefore a measure of the relative expansion rate between the (fastly expanding) under-dense and (slowly expanding) over-dense regions of the model. The effective curvature parameter has roughly the same structure as \mathfrak{Q} . The jerk parameter is dominated by a quadrupole and 16-pole whereas the snap parameter is dominated by a dipole, octupole, and 32-pole. Similar variations in the cosmographic parameters are observed for all other observers across both models.

These observations are all generally expected from the theoretical cosmography expression [7], and similar sky patterns were found (up to 3rd order in the cosmography) for typical observers in the Einstein Toolkit simulations in [9].

5.2 Comparison of ray traced and cosmographic luminosity-distances

In fig. 3, we display the ray traced d_L in models 1 and 2 at five snapshots of redshift. We see that the dominant feature in both plots are a quadrupolar and a dipolar feature, as are the expected main contributions from \mathfrak{H} and \mathfrak{Q} respectively, as discussed in section 5.1.

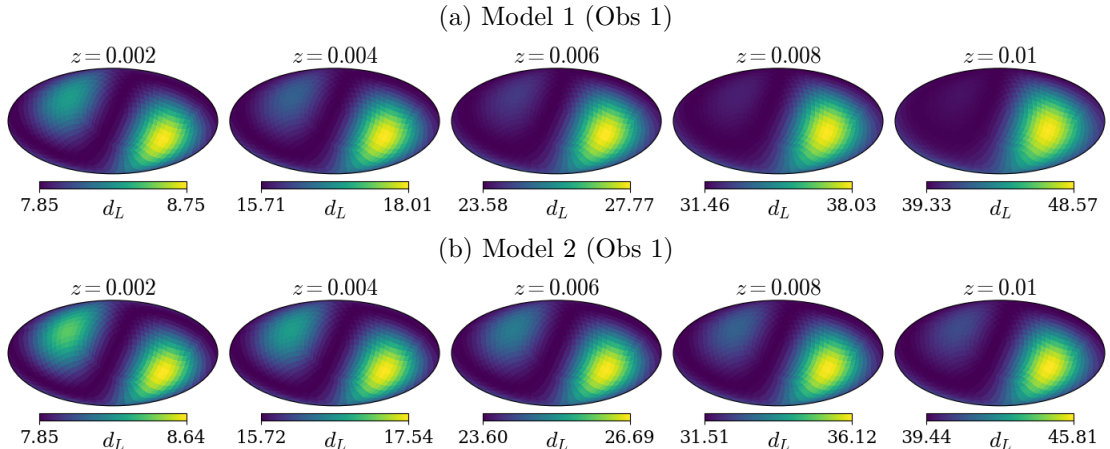


Figure 3. Variation of the ray traced d_L for observer 1 in models 1 and 2. This is presented as full sky maps for hypothetical sources at five equally spaced redshifts between $z = 0.002$ and $z = 0.01$, with the observer located at $z = 0$.

To assess the estimation ability of the covariant cosmographic expansion at each order, we produce full sky maps of the normalised differences between the cosmographic luminosity distance, $d_{L(\text{cosmo})}$, and the ray traced luminosity distance, $d_{L(\text{RT})}$, at increasing redshift intervals from a given observer,

$$\Delta d_L = \frac{d_{L(\text{cosmo})} - d_{L(\text{RT})}}{d_{L(\text{RT})}}. \quad (5.1)$$

The normalized residuals Δd_L for observer 1 for five increasing snapshots of redshift are shown in fig. 4 for model 1 and fig. 5 for model 2. At 1st order in the cosmographic expansion, we see in figs. 4a and 5a that the leading order term in the cosmography, z/\mathfrak{H} , has been successful in accounting for the low-redshift quadrupolar features. Thus, the normalized residuals shown in figs. 4a and 5a are dominated by dipolar contributions. In figs. 4b and 5b it is in turn seen that these dipoles are accounted for by the 2nd order cosmographic term, which is indeed dominated by a dipole through \mathfrak{Q} ; cf. the discussion in section 5.1. We see in fig. 8 that the dipoles in density contrast

$$\Delta\rho = \frac{\rho - \rho_{bg}}{\rho_{bg}}, \quad (5.2)$$

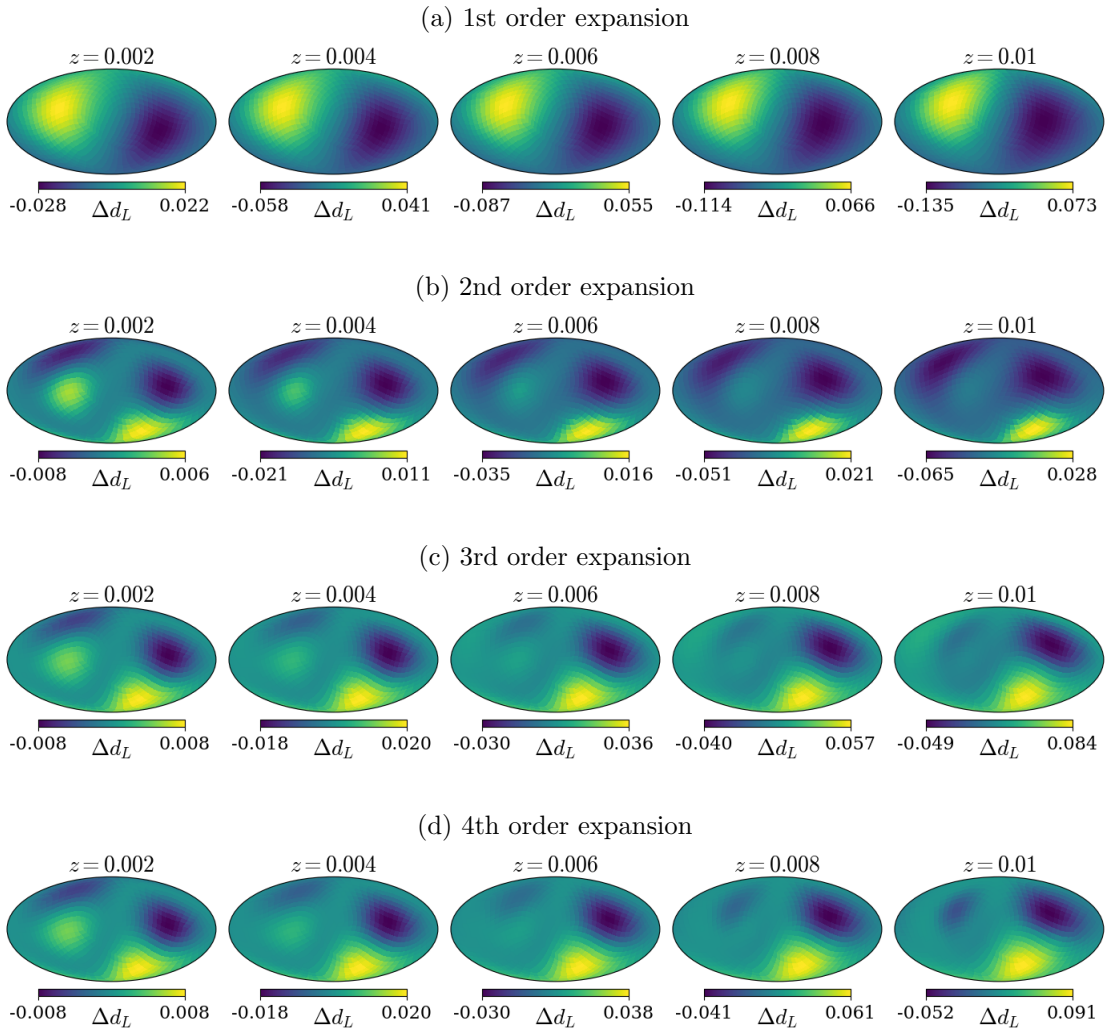


Figure 4. *Model 1* Variation of Δd_L (5.1) up to 4th order in the covariant cosmographic expansion estimate of d_L versus the exact d_L obtained via ray tracing for observer 1 in model 1. This is presented as full sky maps for hypothetical sources at five equally spaced redshifts between $z = 0.002$ and $z = 0.01$, with the observer located at $z = 0$.

where ρ_{bg} is the background density, align with the dipolar axes seen in fig. 3 and in \mathfrak{Q} in fig. 2. This is consistent with the interpretation that the dipole in \mathfrak{Q} is sourced by contrasts in the expansion rate Θ which is again sourced by density contrasts. In the case of both models, Δd_L shows convergence at 2nd order for low redshifts without noticeable improvements when including the 3rd and 4th order terms. At the larger redshift values shown, up to $z = 0.01$, convergence of the cosmographic series by the 4th order is strongly suggested by the similarity of the 3rd and 4th order Δd_L values, especially for model 2. The residual Δd_L does not vanish, however, even for the lowest redshifts, where Δd_L

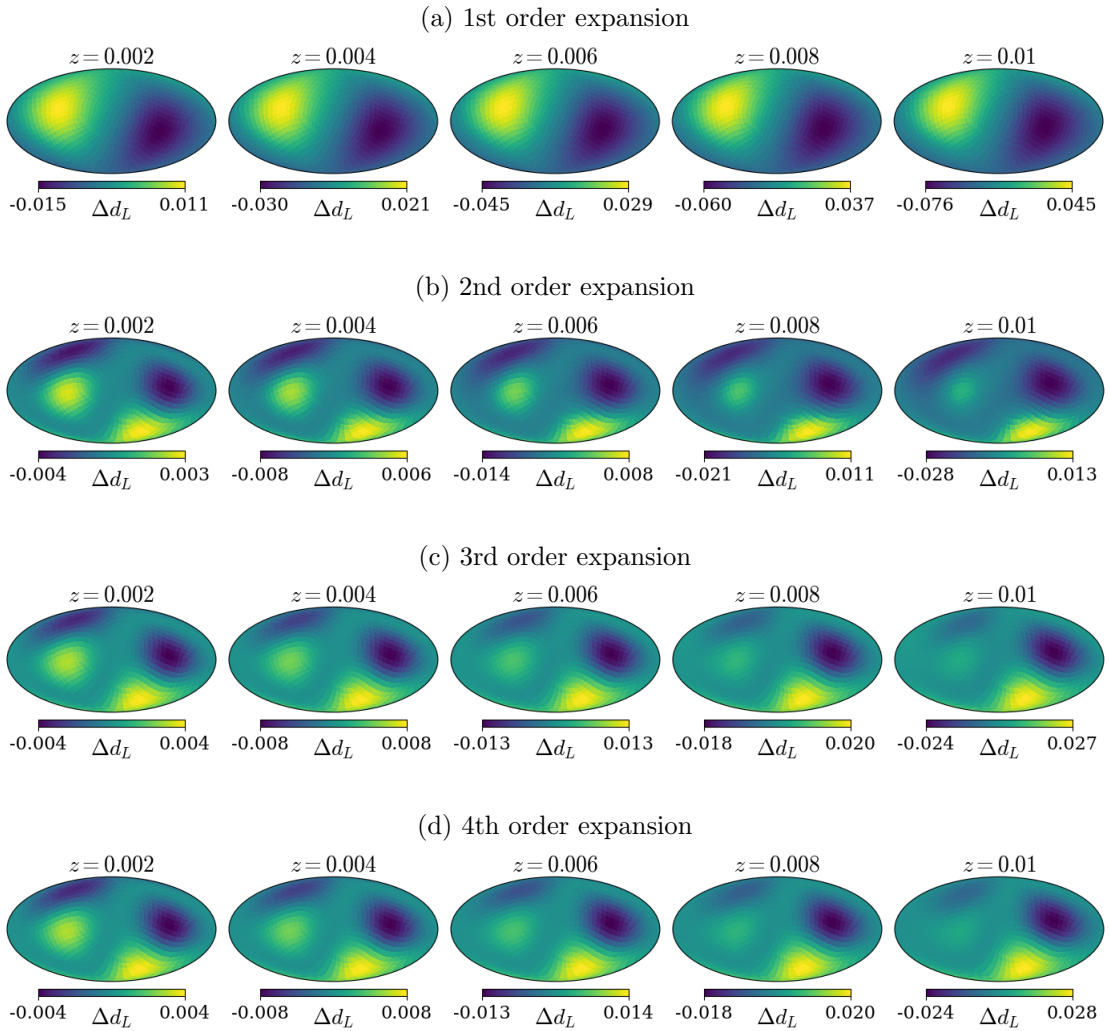


Figure 5. *Model 2* Variation of Δd_L (5.1) up to 4th order in the covariant cosmographic expansion estimate of d_L versus the exact d_L obtained via ray tracing for observer 1 in model 2. This is presented as full sky maps for hypothetical sources at five equally spaced redshifts between $z = 0.002$ and $z = 0.01$, with the observer located at $z = 0$.

takes values of $\lesssim 0.8\%$ for model 1 and $\lesssim 0.4\%$ for model 2, although the mean of the sky map is very close to 0% in both models. At $z = 0.01$, larger residual values of up to $|\Delta d_L| \lesssim 9\%$ for model 1 and $\lesssim 3\%$ for model 2 are observed, again remaining mostly consistent between the 3rd and 4th order. We exclude the numerical resolution in our ray-trace methods as a source of these small observed residuals in appendix A. Rather, these likely arise from the small numerical errors associated with solving for the metric function $R(t, r)$ of the Szekeres solution. The cosmography calculations in particular are very sensitive to numerical errors in the solution for the metric components, as the

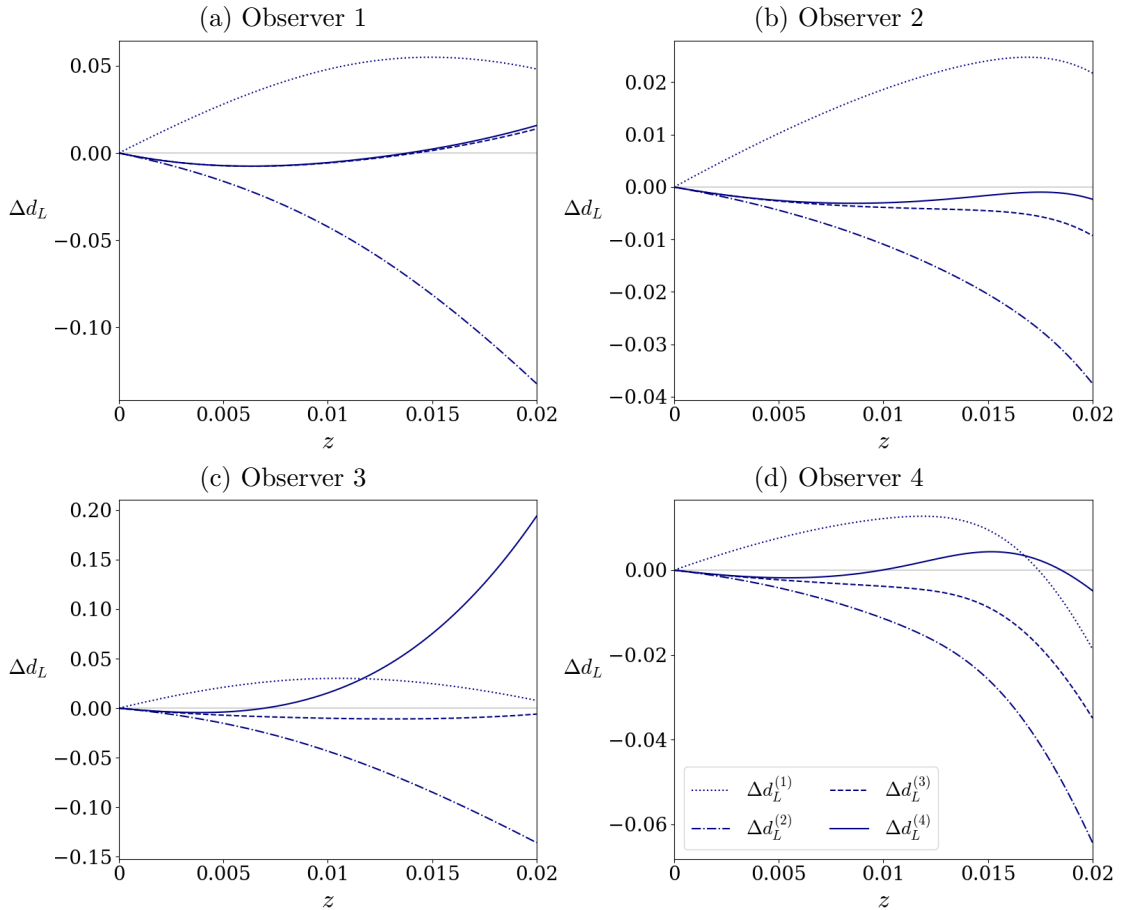


Figure 6. The convergence of Δd_L up to 4th order along a selected test ray with direction coordinates $(\ell, b) = (0.47\pi, 0.81\pi)$ on the sky of each observer in model 1.

increasing number of derivatives for each cosmographic order tends to amplify errors that may otherwise be modest at the metric level.

Although we have primarily discussed our analysis with regards to observer 1, we have performed the exact same analysis with consistent results for the other 3 observers given in table 1. Thus, to provide a snapshot of the full variation of Δd_L with redshift across all observer and model combinations, we show Δd_L at all orders for a single randomly selected ray in figs. 6 and 7 for model 1 and model 2, respectively. To summarise for observers 2, 3 and 4 at the lowest redshift $z \sim 0.002$, we find an overall variation in the maximum 4th order residual of $|\Delta d_L| \lesssim 0.5\%$ for model 1 and 2. As for observer 1, we thus see convergence of the cosmography towards values very similar to the ray traced results, although the residual is not precisely zero, which we ascribe to numerical errors as for observer 1. For these same observers at $z \sim 0.01$, we then find an overall variation in the maximum 4th order residual of $|\Delta d_L| \lesssim 2\%$ for both models. At redshifts $z \sim 0.02$, we then find $|\Delta d_L| \lesssim 20\%$, although most observers/rays perform significantly better

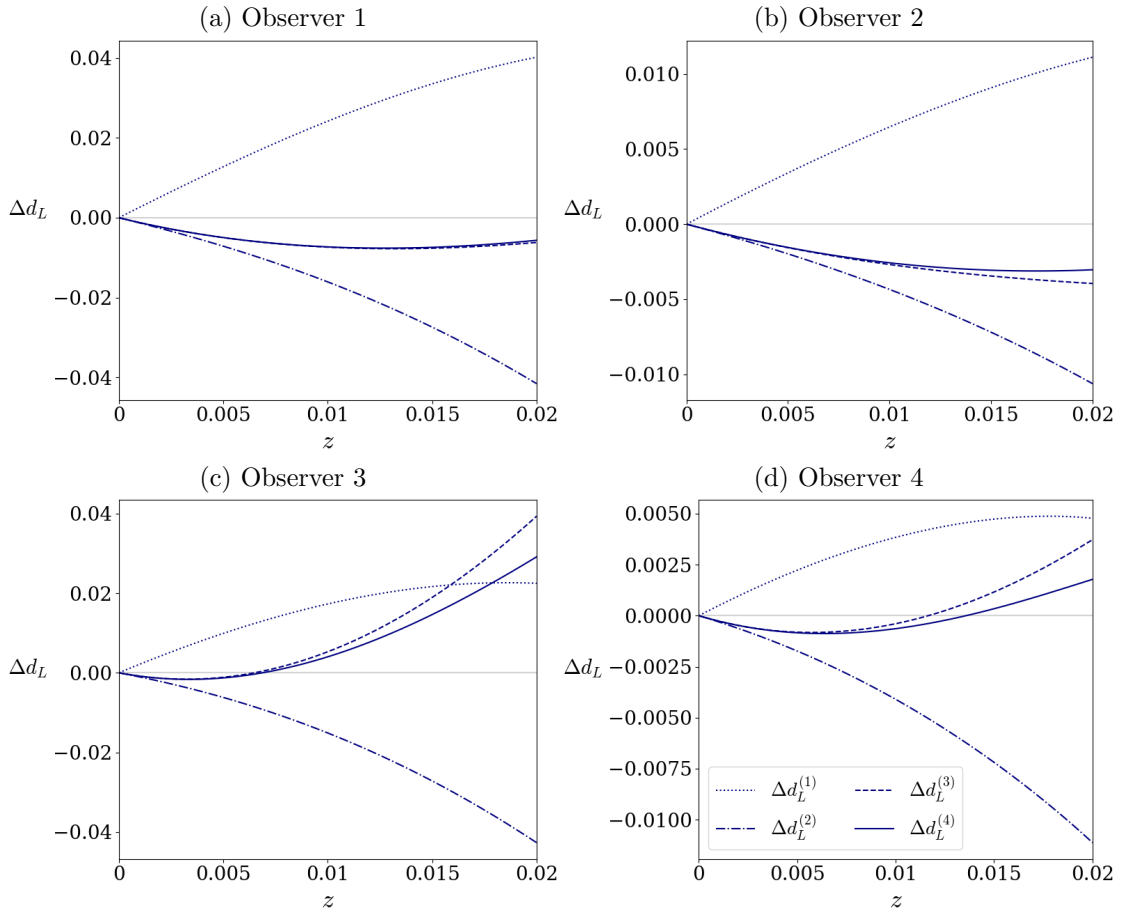


Figure 7. The convergence of Δd_L up to 4th order along a selected test ray with direction coordinates $(\ell, b) = (0.47\pi, 0.81\pi)$ on the sky of each observer in model 2.

with $|\Delta d_L| \lesssim 1\%$ errors. We observe that the 3rd and 4th order approximations give roughly consistent results at scales $z \lesssim 0.01$, after which the different orders of the series tend to part. These results are consistent with those of observer 1, and observers 2, 3, and 4 also have similar full sky distributions to those of observer 1 in figs. 4 and 5. We conclude that the 4th order approximation remains very reliable (up to small numerical errors) out to roughly $z \sim 0.01$, after which more terms in the series are needed for a precise (better than 2% or 5% accurate, dependent on the model) approximation.

5.3 Assessment of Padé Approximants

We assessed the convergence behaviour of the [1/2], [1/3], [2/1], [2/2] and [3/1] Padé approximants outlined in section 2.3. Additionally, we assessed the [3/2] approximant despite it being technically under-determined for the 4th order expansion of $d_L(z)$ (as $M + N > 4$). We find that while the low redshift behaviour of individual rays suggests that some Padé approximants provide a better fit to ray tracing than the standard

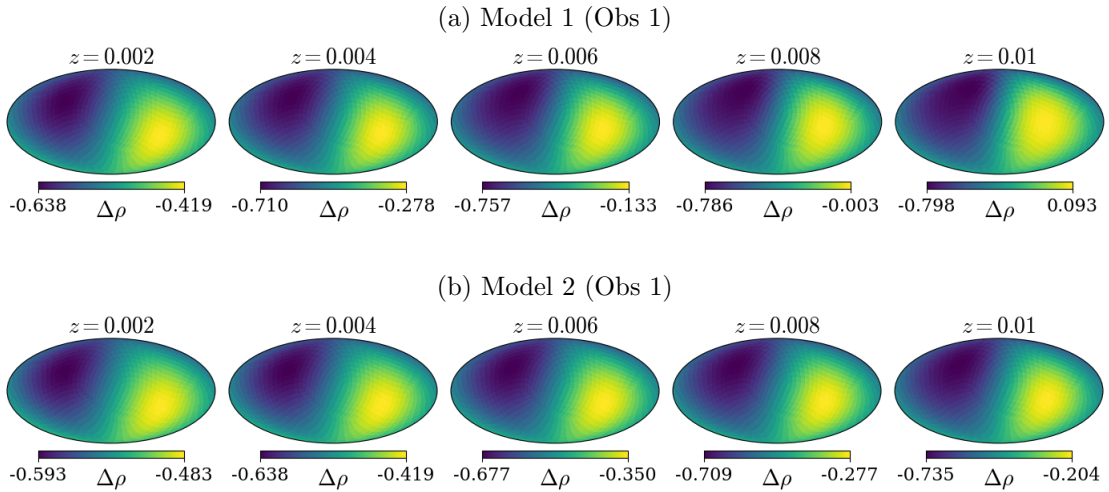


Figure 8. The density contrast $\Delta\rho$ (5.2) measured at the redshift position of each hypothetical source for observer 1 in models 1 and 2, for five equally spaced redshifts between $z = 0.002$ and $z = 0.01$, with the observer located at $z = 0$.

series expansion, the improvement is largely lost at higher redshifts, with the standard expansion often performing marginally better here. However, a robust conclusion on the performances of Padé approximants beyond third order would require control of the residual numerical errors in our analysis discussed in section 5.2.

An overall preference for the [2/1] Padé approximant was previously noted by Capozziello *et al.* [23] for the isotropic FLRW cosmography. The reason that this particular approximant outperformed the [3/2] and [3/1] alternatives is due to degeneracies among the series coefficients when the order $M + N$ of the expansion gets larger. In particular, increasing the number of terms in the denominator increases the occurrence of poles in the approximation. This conclusion agrees with our findings, with the best performance coming from the [2/1] Padé approximant, closely followed by the [3/1] approximant. Moreover, both of these approximants appear free from poles along all discrete lines of sight, which was not the case for all other Padé approximants considered ([1/2], [1/3], [2/2] and [3/2]).

Alternative approximations which may be considered in future work include the Chebyshev polynomials investigated in [22], which were found to generally perform better than the associated higher order Padé and Taylor series expansions. Importantly, the Chebyshev approximant features all higher order terms of the corresponding Taylor series, including those containing the snap parameter \mathfrak{S} , within its lower order terms. This is in contrast to range of valid ($M + N \leq 4$) Padé approximants for the 4th order cosmography, which by construction cannot contain the 4th order terms involving the snap parameter. Finally, one might also consider an alternative distance-redshift expansion, such as the inverse series $z(d_L)$ or $z(d_A)$ in conjunction with a suitable alternative approximant, as was done in [16, 35].

6 Discussion and conclusion

In our analysis, we find that the covariant cosmography expansions as applied to our Λ -Szekeres models have somewhat low- z radii within which the 4th order expansion remains a reliable predictor for the exact ray traced luminosity distance–redshift relation, with the 4th order series starting to diverge when approaching the edge of the structure. This is consistent with previous findings in numerical relativity simulations and LTB models [9, 10, 25], indicating that low-order cosmographies tend to be reliable only within distances corresponding to the characteristic sizes of the structures in the space-time. We note that the level of approximation of the cosmography are highly sensitive to the chosen density profile of the structure. We found that alternative non-analytic parameterisations or choices of parameterisations with more extreme localised spatial gradients than our canonical Gaussian density profile (3.13) generally resulted in less accurate cosmographies as one may have expected. This is again compatible with the findings in [9, 10, 25]. The main limitation of our analysis is the presence of numerical errors in solving for the Szekeres metric function $R(t, r)$ and their propagation to the calculated d_L - z relation. Other sources of errors, such as the finite resolution in the ray tracing were shown to be negligible. We expect our overall conclusions to be robust towards improvements in numerical accuracy, and the level of approximation/convergence results that we have presented in this paper for the 4th order cosmography can be taken as conservative estimates.

Generalised cosmography has been investigated in multiple prior studies, and we comment on those most relevant to our investigations here. The investigation presented in this paper may be contrasted to those presented by Modan & Koksbang in [24] (Hereafter referred to as MK24), who performed a similar analysis using cosmographic formalism for LTB models. In particular, they compare the covariant cosmographic expansion to third order in redshift for LTB models to results obtained via general relativistic ray tracing in the models. A key finding was the convergence of the cosmographic series at low radii/redshifts to the ray traced results, which supports our hypothesis that the small residuals of the cosmography relative to the ray traced results towards very small redshifts are due to small numerical errors in our solving for the metric rather than signifying inaccuracy in the cosmographic approach.

In MK24, the radii of convergence of the 3rd order cosmography for all models and observers they consider were well within the confines of the LTB structures, which is consistent with the findings of this work. Another paper by Sarma *et al.* on LTB structures [25] arrived at similar conclusions to MK24, with the radii of convergence of the 3rd cosmography being within the confines of investigated LTB structures. These results, as is also noted in [25], suggest that care must be taken in interpreting the results when fitting the cosmographic series to data that span multiple structures: We should not expect to arrive at the analytic cosmographic variables derivable from derivatives in a local space-time metric that precisely describe every structure. Rather, the inferred cosmographic parameters should be seen as average parameters that appropriately describe the survey domain. This was also noted in [50], where an interpretation

of cosmographic parameters (specifically the dipole in the distance-redshift law) were given in terms of *average* space-time variables, thus extending the convergence of the cosmographic prediction.

In depth investigations of cosmography as employed to synthetic observers within realistic numerical relativity simulations for cosmology were carried out using the Einstein Toolkit and *gevolution* simulations [9, 10, 35]. These investigations mainly focused on mapping the large-scale universe above distance scales of $100 - 200 h^{-1}$ Mpc. Thus, with our focus on local structures around scales of $100 h^{-1}$ Mpc in radii, the investigations in this paper represent complementary investigations to the previously carried out simulation studies.

It is intriguing that a recent analysis of the CosmicFlows4 dataset by Kalbouneh *et al.* [15] utilizing covariant cosmography found significant anisotropies, dominated by a dipole, in our local cosmic neighbourhood $z \lesssim 0.1$ which are in tension with the Λ CDM model at the 3σ -level; see also [51] for an alternative approach that arrives at a similar significance level. The results in [15] moreover point to axisymmetry of the underlying solution, and thus the axisymmetric Szekeres solutions that we have investigated in this paper may provide a class of models which are interesting for examining data from the local Universe.

Acknowledgments

We thank Timothy Clifton and Sofie Koksbang for helpful discussions, and Pierre Mourier and David Wiltshire for detailed comments on drafts of the manuscript. This work was partly supported by Marsden Fund grant M1271 administered by the Royal Society of New Zealand, Te Apārangi. MH also wishes to thank Zachary Lane, Marco Galoppo and Shreyas Tiruvaskar for insightful discussions and comments. AH also acknowledges the Perren Fund from the University of London and the Astronomy Unit at Queen Mary University of London for their support.

A Numerical Convergence & Accuracy

Throughout our analysis, we have performed a variety of assessments for the stability and accuracy of both the ray tracing and cosmographic solutions. A substantial component of our codes is the ray tracing algorithms, which utilise the ODE solvers of the `DifferentialEquations.jl` package. There are various means for controlling the behaviour of the solver, including the setting of the step size control parameters. One of these parameters is the maximum step size performed by the adaptive ‘time-stepping’ algorithm, which is equivalent to varying the maximum allowed step size of the affine parameter, $\Delta\lambda_{\max}$, in our numerical routines which integrate the null geodesic equations (which were discussed in section 4).

To check that the solutions generated by these routines are not variable with this choice of step size, and to gauge if similar control options may affect the results, we have performed our ray tracing analysis scheme for a sample of observer and model

combinations while varying $\Delta\lambda_{\max}$. For each test case, we individually examine 12 rays evenly spread across the observer's sky⁵, by assessing Δd_L over the full redshift along a given ray for $0.001 \leq \Delta\lambda_{\max}/\text{Mpc} \leq 8.0$ – including the $\Delta\lambda_{\max}/\text{Mpc} = 1.0$ used in our results. Overall, we find that Δd_L varies insignificantly across the range of $\Delta\lambda_{\max}$ tested, indicating that convergence is already achieved when tracing rays with $\Delta\lambda_{\max}/\text{Mpc} = 1.0$. Examination of the individual rays with different $\Delta\lambda_{\max}$ yeilds virtually indentical result plots similar to figs. 6 and 7. Thus, any minute variations are much smaller than the residual Δd_L values of order $\mathcal{O}(10^{-2})$ that we obtained between ray traced and 4th order cosmographic expansion estimates (see fig. 4 and fig. 5). We thus conclude that these residual values should not be due to numerical convergence issues of ray tracing routines themselves.

In addition to the numerical convergence testing of the ray tracing routines, further performance and stability tests were performed for routines which acquire and take numerical derivatives of certain key functions e.g., those within (3.4) and (2.3). This is because the computation of cosmographic parameters in section 2.2 contain higher order derivatives of metric functions. Overall, we found that our numerical differentiation routines performed well when compared to other candidates explored (e.g., the automatic differentiation procedure we implement for derivatives of $R(t, r)$ with respect to r outperforms manual finite differencing).

B Null vector initialisation procedure

The local orthonormal basis $\{\xi_{\hat{\alpha}}\}$ can be determined by first considering the line element

$$ds^2 = g_{\mu\nu} dx^\mu \otimes dx^\nu = \eta_{\hat{\alpha}\hat{\beta}} \omega^{\hat{\alpha}} \otimes \omega^{\hat{\beta}}, \quad (\text{B.1})$$

where $\eta_{\hat{\alpha}\hat{\beta}} = \text{diag}(-1, 1, 1, 1)$ and $\{\omega^{\hat{\alpha}}\}$ are the 1-forms dual to the orthonormal basis, such that

$$\omega^{\hat{\alpha}}(\xi_{\hat{\beta}}) = \omega^{\hat{\alpha}}_\mu \xi^\mu_{\hat{\beta}} = \delta^{\hat{\alpha}}_{\hat{\beta}}. \quad (\text{B.2})$$

By extracting the 1-forms of the Szekeres line element in spherical coordinates (3.7), we can solve (B.2) to obtain the following orthonormal basis

$$\xi^{\mu}_{\hat{\alpha}} = \begin{pmatrix} 1 & 0 & 0 & 0 \\ 0 & \zeta & 0 & 0 \\ 0 & \zeta \frac{S' \sin \theta + \mathcal{N}(1 - \cos \theta)}{S} & \frac{1}{R} & 0 \\ 0 & -\zeta \frac{(\partial_\phi \mathcal{N})(1 - \cos \theta)}{S \sin \theta} & 0 & \frac{1}{R \sin \theta} \end{pmatrix}, \quad (\text{B.3})$$

where

$$\zeta = \sqrt{1 - k} \left[R' + \frac{R}{S} (S' \cos \theta + \mathcal{N} \sin \theta) \right]^{-1}. \quad (\text{B.4})$$

⁵As we use HEALPix to define our inital ray directions, 12 rays correspond to the minimum pixel resolution of HEALPix map.

As we have $k_{\text{obs}}^{\hat{\alpha}} = (1, -\hat{\mathbf{n}})$ in the local orthonormal frame, with the components of $\hat{\mathbf{n}}$ defined in (4.5), our initial null vector at the event of observation k_{obs}^{μ} is

$$k_{\text{obs}}^{\mu} = \xi^{\mu}_{\hat{\alpha}} k^{\hat{\alpha}} \Big|_{\text{obs}} = \begin{pmatrix} 1 \\ -\zeta \hat{n}^x \\ -\zeta \frac{S' \sin \theta + \mathcal{N}(1 - \cos \theta)}{S} \hat{n}^x - \frac{1}{R} \hat{n}^y \\ \zeta \frac{(\partial_{\phi} \mathcal{N})(1 - \cos \theta)}{S \sin \theta} \hat{n}^x - \frac{1}{R \sin \theta} \hat{n}^z \end{pmatrix}_{\text{obs}}. \quad (\text{B.5})$$

In the special case of axisymmetry, the above simplifies with $\mathcal{N} = 0$.

C Evolution of the direction vector of the photon congruence

In order to compute higher order derivatives of \mathfrak{H} , as needed to obtain the cosmographic expressions, one must necessarily compute the corresponding derivatives of e^{μ} . The first derivative yields (cf. also [7]),

$$\frac{D e^{\mu}}{d\lambda} = E(e^{\mu} - u^{\mu})\mathfrak{H} - Ee^{\nu} \left(\frac{1}{3} \Theta h^{\mu}_{\nu} + \sigma^{\mu}_{\nu} \right), \quad (\text{C.1})$$

where we have used the geodesic equation and the decomposition in (2.4). The second and third covariant derivatives of the direction vector are respectively given by

$$\begin{aligned} \frac{D^2 e^{\mu}}{d\lambda^2} &= E^2 \mathfrak{H} \left(\frac{1}{3} \Theta e^{\mu} + (e^{\nu} - u^{\nu}) \sigma^{\mu}_{\nu} \right) - \frac{1}{3} E \left(e^{\mu} \frac{d\Theta}{d\lambda} + \Theta \frac{D e^{\mu}}{d\lambda} \right) \\ &\quad + E(e^{\mu} - u^{\mu}) \frac{d\mathfrak{H}}{d\lambda} - E \left(\sigma^{\mu}_{\nu} \frac{D e^{\nu}}{d\lambda} + e^{\nu} \frac{D \sigma^{\mu}_{\nu}}{d\lambda} \right), \end{aligned}$$

$$\begin{aligned} \frac{D^3 e^{\mu}}{d\lambda^3} &= E \frac{d\mathfrak{H}}{d\lambda} \frac{D e^{\mu}}{d\lambda} - 2E \mathfrak{H} \frac{D^2 e^{\mu}}{d\lambda^2} + \frac{2}{3} E^2 \Theta \frac{d\mathfrak{H}}{d\lambda} e^{\mu} - \frac{2}{3} E \frac{d\Theta}{d\lambda} \frac{D e^{\mu}}{d\lambda} - \frac{1}{3} E \Theta \frac{D^2 e^{\mu}}{d\lambda^2} \\ &\quad - E \sigma^{\mu}_{\nu} \frac{D^2 e^{\nu}}{d\lambda^2} - E^2 \mathfrak{H} \frac{D \sigma^{\mu}_{\nu}}{d\lambda} u^{\nu} - 2E \frac{D e^{\nu}}{d\lambda} \frac{D \sigma^{\mu}_{\nu}}{d\lambda} + \frac{1}{3} E^3 \mathfrak{H} \Theta e^{\nu} \sigma^{\mu}_{\nu} \\ &\quad + E(e^{\mu} - u^{\mu}) \frac{d^2 \mathfrak{H}}{d\lambda^2} + E^2 \mathfrak{H} (e^{\mu} - u^{\mu}) \frac{d\mathfrak{H}}{d\lambda} + 2E^2 e^{\nu} \sigma^{\mu}_{\nu} \frac{d\mathfrak{H}}{d\lambda} \\ &\quad + E^3 \mathfrak{H} e^{\nu} \sigma^{\mu}_{\gamma} \sigma^{\gamma}_{\nu} - \frac{1}{3} E e^{\mu} \frac{d^2 \Theta}{d\lambda^2} - E e^{\nu} \frac{D^2 \sigma^{\mu}_{\nu}}{d\lambda^2}, \end{aligned}$$

where we have used $u^{\mu} u_{\mu} = -1$, $e^{\mu} u_{\mu} = 0$, $k^{\mu} \nabla_{\mu} k^{\nu} = 0$ in the derivations, as well as appropriate substitutions of (2.1), (2.2) and (C.1).

D Metric Derived Quantities

Here we list the non-zero Christoffel symbols and the Ricci tensor for the Szekeres model under investigation, along with the derivatives of the dipole function that enter the Ricci tensor.

D.1 Non-Zero Christoffel Symbols

$$\Gamma^t_{rr} = -\frac{(R'\mathcal{E} - R\mathcal{E}') \left(\dot{R}'\mathcal{E} - \dot{R}\mathcal{E}' \right)}{(k-1)\mathcal{E}^2}, \quad \Gamma^t_{pp} = \Gamma^t_{qq} = \frac{R\dot{R}}{\mathcal{E}^2},$$

$$\Gamma^r_{tr} = \Gamma^r_{rt} = \frac{\dot{R}'\mathcal{E} - \dot{R}\mathcal{E}'}{R'\mathcal{E} - R\mathcal{E}'}, \quad \Gamma^r_{pp} = \Gamma^r_{qq} = \frac{(k-1)R}{\mathcal{E}(R'\mathcal{E} - R\mathcal{E}')},$$

$$\begin{aligned} \Gamma^r_{rr} = \frac{1}{2\mathcal{E}(R'\mathcal{E} - R\mathcal{E}')(k-1)} & \left[\mathcal{E} [\mathcal{E}' (k'R - 2(k-1)R') - 2(k-1)R\mathcal{E}'''] \right. \\ & \left. + \mathcal{E}^2 (2(k-1)R'' - k'R') + 2(k-1)R\mathcal{E}'^2 \right], \end{aligned}$$

$$\Gamma^r_{rp} = \Gamma^r_{pr} = \frac{R((\partial_p\mathcal{E})\mathcal{E}' - \mathcal{E}(\partial_p\mathcal{E}'))}{\mathcal{E}(R'\mathcal{E} - R\mathcal{E}')}, \quad \Gamma^r_{rq} = \Gamma^r_{qr} = \frac{R((\partial_q\mathcal{E})\mathcal{E}' - \mathcal{E}(\partial_q\mathcal{E}'))}{\mathcal{E}(R'\mathcal{E} - R\mathcal{E}')},$$

$$\Gamma^p_{tp} = \Gamma^p_{pt} = \frac{\dot{R}}{R}, \quad \Gamma^p_{rr} = \frac{(\mathcal{E}(\partial_p\mathcal{E}') - (\partial_p\mathcal{E})\mathcal{E}')(R\mathcal{E}' - R'\mathcal{E})}{(k-1)R\mathcal{E}},$$

$$\Gamma^p_{rp} = \Gamma^p_{pr} = \frac{R'}{R} - \frac{\mathcal{E}'}{\mathcal{E}}, \quad \Gamma^p_{pp} = -\Gamma^p_{qq} = -\frac{(\partial_p\mathcal{E})}{\mathcal{E}}, \quad \Gamma^p_{pq} = \Gamma^p_{qp} = -\frac{(\partial_q\mathcal{E})}{\mathcal{E}},$$

$$\Gamma^q_{tq} = \Gamma^q_{qt} = \frac{\dot{R}}{R}, \quad \Gamma^q_{rr} = \frac{(\mathcal{E}(\partial_q\mathcal{E}') - (\partial_q\mathcal{E})\mathcal{E}')(R\mathcal{E}' - R'\mathcal{E})}{(k-1)R\mathcal{E}},$$

$$\Gamma^q_{rq} = \Gamma^q_{qr} = \frac{R'}{R} - \frac{\mathcal{E}'}{\mathcal{E}}, \quad \Gamma^q_{pq} = \Gamma^q_{qp} = -\frac{(\partial_p\mathcal{E})}{\mathcal{E}},$$

$$\Gamma^q_{qq} = -\Gamma^q_{pp} = -\frac{(\partial_q\mathcal{E})}{\mathcal{E}}.$$

D.2 Non-Zero Components of the Ricci Tensor

$$R_{tt} = \frac{\ddot{R}\mathcal{E}' - \ddot{R}'\mathcal{E}}{R'\mathcal{E} - R\mathcal{E}'} - \frac{2\ddot{R}}{R},$$

$$\begin{aligned} R_{rr} = \frac{-(R'\mathcal{E} - R\mathcal{E}')}{(k-1)R\mathcal{E}^2} & \left[\mathcal{E}' \left(2 \left[(\partial_q\mathcal{E})^2 + (\partial_p\mathcal{E})^2 + 1 \right] - 2\dot{R}^2 - R\ddot{R} - 2k \right) \right. \\ & + \mathcal{E} \left(-(\partial_{qq}\mathcal{E} + \partial_{pp}\mathcal{E})\mathcal{E}' - 2 \left[(\partial_q\mathcal{E})(\partial_q\mathcal{E}') + (\partial_p\mathcal{E})(\partial_p\mathcal{E}') \right] + 2\dot{R}\dot{R}' + R\ddot{R}' + k' \right) \\ & \left. + (\partial_{qq}\mathcal{E}' + \partial_{pp}\mathcal{E}')\mathcal{E}^2 \right], \end{aligned}$$

$$\begin{aligned}
R_{pp} &= \frac{1}{2\mathcal{E}^2} \left[\frac{R}{R'\mathcal{E} - R\mathcal{E}'} \left[\mathcal{E} \left(-2[(\partial_{pp}\mathcal{E})\mathcal{E}' + (\partial_q\mathcal{E})(\partial_q\mathcal{E}') + (\partial_p\mathcal{E})(\partial_p\mathcal{E}')] + 2\dot{R}\dot{R}' + k' \right) \right. \right. \\
&\quad \left. \left. + 2\mathcal{E}' \left((\partial_q\mathcal{E})^2 + (\partial_p\mathcal{E})^2 - \dot{R}^2 - k + 1 \right) + 2(\partial_{pp}\mathcal{E}')\mathcal{E}^2 \right] \right. \\
&\quad \left. + 2 \left(-(\partial_q\mathcal{E})^2 - (\partial_p\mathcal{E})^2 + \mathcal{E}(\partial_{qq}\mathcal{E} + \partial_{pp}\mathcal{E}) + \dot{R}^2 + k - 1 \right) + 2R\ddot{R} \right], \\
R_{qq} &= \frac{1}{2\mathcal{E}^2} \left[\frac{R}{R'\mathcal{E} - R\mathcal{E}'} \left[\mathcal{E} \left(-2[(\partial_{qq}\mathcal{E})\mathcal{E}' + (\partial_q\mathcal{E})(\partial_q\mathcal{E}') + (\partial_p\mathcal{E})(\partial_p\mathcal{E}')] + 2\dot{R}\dot{R}' + k' \right) \right. \right. \\
&\quad \left. \left. + 2\mathcal{E}' \left((\partial_q\mathcal{E})^2 + (\partial_p\mathcal{E})^2 - \dot{R}^2 - k + 1 \right) + 2(\partial_{qq}\mathcal{E}')\mathcal{E}^2 \right] \right. \\
&\quad \left. + 2 \left(-(\partial_q\mathcal{E})^2 - (\partial_p\mathcal{E})^2 + \mathcal{E}(\partial_{qq}\mathcal{E} + \partial_{pp}\mathcal{E}) + \dot{R}^2 + k - 1 \right) + 2R\ddot{R} \right].
\end{aligned}$$

D.3 Derivatives of the Szekeres dipole function

$$\begin{aligned}
\mathcal{E} &= \frac{(p - P)^2 + (q - Q)^2 + S^2}{2S}, \\
\mathcal{E}' &= -2 \frac{(p - P)P' + (q - Q)Q' - SS'}{(p - P)^2 + (q - Q)^2 + S^2} \mathcal{E} - \frac{S'}{S} \mathcal{E}, \\
\mathcal{E}'' &= S'' \left(1 - \frac{\mathcal{E}}{S} \right) + 2\mathcal{E} \left(\frac{S'}{S} \right)^2 + \frac{2((p - P)P' + (q - Q)Q')S'}{S^2} \\
&\quad + \frac{P'^2 + Q'^2 - S'^2 - (p - P)P'' - (q - Q)Q''}{S}, \\
\partial_p\mathcal{E} &= \frac{p - P}{S}, \quad \partial_p\mathcal{E}' = -\frac{SP' + (p - P)S'}{S^2}, \\
\partial_q\mathcal{E} &= \frac{q - Q}{S}, \quad \partial_q\mathcal{E}' = -\frac{SQ' + (q - Q)S'}{S^2}, \\
\partial_{pp}\mathcal{E} &= \partial_{qq}\mathcal{E} = \frac{1}{S}, \quad \partial_{pp}\mathcal{E}' = \partial_{qq}\mathcal{E}' = -\frac{S'}{S^2}.
\end{aligned}$$

References

- [1] S. Weinberg, *Gravitation and Cosmology: Principles and Applications of the General Theory of Relativity*, John Wiley and Sons, New York (1972).
- [2] G.F.R. Ellis, S.D. Nel, R. Maartens, W.R. Stoeger and A.P. Whitman, *Ideal observational cosmology*, *Phys. Rep.* **124** (1985) 315.
- [3] M. Visser, *Cosmography: Cosmology without the Einstein equations*, *Gen. Rel. Grav.* **37** (2005) 1541 [[gr-qc/0411131](https://arxiv.org/abs/gr-qc/0411131)].

- [4] J. Kristian and R.K. Sachs, *Observations in cosmology*, *Astrophys. J.* **143** (1966) 379.
- [5] O. Umeh, "The influence of structure formation on the evolution of the universe.", Ph.D. thesis, University of Cape Town, Faculty of Science, Department of Mathematics and Applied Mathematics, 2013.
- [6] C. Clarkson, G.F.R. Ellis, A. Faltenbacher, R. Maartens, O. Umeh and J.-P. Uzan, (Mis-)Interpreting supernovae observations in a lumpy universe, *Mon. Not. Roy. Astron. Soc.* **426** (2012) 1121 [[1109.2484](#)].
- [7] A. Heinesen, *Multipole decomposition of the general luminosity distance 'Hubble law' – a new framework for observational cosmology*, *JCAP* **05** (2021) 008 [[2010.06534](#)].
- [8] B. Kalbouneh, C. Marinoni and R. Maartens, *Cosmography of the Local Universe by Multipole Analysis of the Expansion Rate Fluctuation Field*, *JCAP* **09** (2024) 069 [[2401.12291](#)].
- [9] H.J. Macpherson and A. Heinesen, *Luminosity distance and anisotropic sky-sampling at low redshifts: A numerical relativity study*, *Phys. Rev. D* **104** (2021) 023525 [[2103.11918](#)].
- [10] H.J. Macpherson, *Cosmological distances with general-relativistic ray tracing: framework and comparison to cosmographic predictions*, *JCAP* **03** (2023) 019 [[2209.06775](#)].
- [11] J. Adamek, C. Clarkson, R. Durrer, A. Heinesen, M. Kunz and H.J. Macpherson, *Towards Cosmography of the Local Universe*, *Open J. Astrophys.* **7** (2024) 001c.118782 [[2402.12165](#)].
- [12] J. Colin, R. Mohayaee, M. Rameez and S. Sarkar, *Evidence for anisotropy of cosmic acceleration*, *Astron. Astrophys.* **631** (2019) L13 [[1808.04597](#)].
- [13] S. Dhawan, A. Borderies, H.J. Macpherson and A. Heinesen, *The quadrupole in the local Hubble parameter: first constraints using Type Ia supernova data and forecasts for future surveys*, *Mon. Not. Roy. Astron. Soc.* **519** (2023) 4841 [[2205.12692](#)].
- [14] J.A. Cowell, S. Dhawan and H.J. Macpherson, *Potential signature of a quadrupolar hubble expansion in Pantheon+supernovae*, *Mon. Not. Roy. Astron. Soc.* **526** (2023) 1482 [[2212.13569](#)].
- [15] B. Kalbouneh, C. Marinoni, R. Maartens, J. Bel, J. Santiago, C. Clarkson et al., *The anisotropic expansion rate of the local Universe and its covariant cosmographic interpretation*, Oct., 2025. 10.48550/arXiv.2510.02510.
- [16] A. Heinesen and M. Korzyński, *Exploring the rich geometrical information in cosmic drift signals with covariant cosmography*, *Phys. Rev. D* **110** (2024) 043525 [[2406.06167](#)].
- [17] F.S.N. Lobo, J.P. Mimoso and M. Visser, *Cosmographic analysis of redshift drift*, *JCAP* **04** (2020) 043 [[2001.11964](#)].
- [18] B.A.R. Rocha and C.J.A.P. Martins, *Redshift drift cosmography with ELT and SKAO measurements*, *Mon. Not. Roy. Astron. Soc.* **518** (2022) 2853 [[2211.02751](#)].
- [19] A. Heinesen, *Redshift drift cosmography for model-independent cosmological inference*, *Phys. Rev. D* **104** (2021) 123527 [[2107.08674](#)].
- [20] M. Quartin and L. Amendola, *Distinguishing between void models and dark energy with cosmic parallax and redshift drift*, *Phys. Rev. D* **81** (2010) 043522 [[0909.4954](#)].
- [21] C. Cattoen and M. Visser, *The Hubble series: Convergence properties and redshift variables*, *Class. Quant. Grav.* **24** (2007) 5985 [[0710.1887](#)].

[22] S. Capozziello, R. D'Agostino and O. Luongo, *Cosmographic analysis with Chebyshev polynomials*, *Mon. Not. Roy. Astron. Soc.* **476** (2018) 3924 [[1712.04380](#)].

[23] S. Capozziello, R. D'Agostino and O. Luongo, *High-redshift cosmography: auxiliary variables versus Padé polynomials*, *Mon. Not. Roy. Astron. Soc.* **494** (2020) 2576 [[2003.09341](#)].

[24] A.B. Modan and S.M. Koksbang, *On the convergence of cosmographic expansions in Lemaître–Tolman–Bondi models*, *Class. Quant. Grav.* **41** (2024) 235018 [[2408.07459](#)].

[25] M. Sarma, C. Marinoni, B. Kalbouneh, C. Clarkson and R. Maartens, *Covariant cosmography in the presence of local structures: comparing exact solutions and perturbation theory*, [2510.03517](#).

[26] N. Meures and M. Bruni, *Redshift and distances in a Λ CDM cosmology with non-linear inhomogeneities*, *Monthly Notices of the Royal Astronomical Society* **419** (2012) 1937 [[1107.4433](#)].

[27] M.-N. Célérier, *Precision cosmology with exact inhomogeneous solutions of general relativity: The Szekeres models*, *Phys. Rev. D* **110** (2024) 123526 [[2407.04452](#)].

[28] G.F.R. Ellis, R. Maartens and M.A.H. MacCallum, *Relativistic Cosmology*, Cambridge University Press, Cambridge, UK (2012).

[29] B. Kalbouneh, J. Santiago, C. Marinoni, R. Maartens, C. Clarkson and M. Sarma, *Expanding covariant cosmography of the local universe: incorporating the snap and axial symmetry*, *JCAP* **02** (2025) 076.

[30] C. Cattoën and M. Visser, *The Hubble series: convergence properties and redshift variables*, *Classical and Quantum Gravity* **24** (2007) 5985.

[31] V.C. Busti, P.K.S. Dunsby, A. de la Cruz-Dombriz and D. Saez-Gomez, *Is cosmography a useful tool for testing cosmology?*, *Physical Review D* **92** (2015) 123512.

[32] S. Nesseris and J. García-Bellido, *Comparative analysis of model-independent methods for exploring the nature of dark energy*, *Physical Review D* **88** (2013) 063521.

[33] D. Sapone, E. Majerotto and S. Nesseris, *Curvature versus distances: Testing the FLRW cosmology*, *Physical Review D* **90** (2014) 023012.

[34] C. Gruber and O. Luongo, *Cosmographic analysis of the equation of state of the universe through Padé approximations*, *Physical Review D* **89** (2014) 103506.

[35] J. Adamek, C. Clarkson, R. Durrer, A. Heinesen, M. Kunz and H.J. Macpherson, *Towards Cosmography of the Local Universe*, *The Open Journal of Astrophysics* **7** (2024) .

[36] G.A. Baker and P.R. Graves-Morris, *Padé Approximants*, Cambridge University Press, 2nd ed. ed. (1996).

[37] W.H. Press, ed., *Numerical Recipes in FORTRAN : The Art of Scientific Computing*, Cambridge University Press, Cambridge England ; New York, 2nd ed. ed. (1992).

[38] H. Bondi, *Spherically Symmetrical Models in General Relativity*, *Monthly Notices of the Royal Astronomical Society* **107** (1947) 410.

[39] R.G. Buckley and E.M. Schlegel, *Physical geometry of the quasispherical Szekeres models*, *Physical Review D* **101** (2020) 023511.

[40] PLANCK collaboration, *Planck 2018 results. VI. Cosmological parameters*, *Astron. Astrophys.* **641** (2020) A6 [[1807.06209](#)].

- [41] K. Bolejko, M.A. Nazer and D.L. Wiltshire, *Differential cosmic expansion and the Hubble flow anisotropy*, *JCAP* **06** (2016) 035.
- [42] S.M. Koksbang and S. Hannestad, *Studying the precision of ray tracing techniques with Szekeres models*, *Physical Review D* **92** (2015) 023532.
- [43] L. Dam, *Inhomogeneous Cosmological Models and the Cosmic Microwave Background*, Master's thesis, University of Canterbury, Christchurch, New Zealand, 2016, <http://dx.doi.org/10.26021/9152>.
- [44] M. Hills, *Ray tracing & averaging in Szekeres cosmological models*, Master's thesis, University of Canterbury, Christchurch, New Zealand, 2022, <http://dx.doi.org/10.26021/12861>.
- [45] A. Zonca, L. Singer, D. Lenz, M. Reinecke, C. Rosset, E. Hivon et al., *healpy: equal area pixelization and spherical harmonics transforms for data on the sphere in Python*, *Journal of Open Source Software* **4** (2019) 1298.
- [46] M. Tomasi and Z. Li, *Healpix.jl: Julia-only port of the HEALPix library*, Sept., 2021.
- [47] C. Rackauckas and Q. Nie, *DifferentialEquations.jl – A Performant and Feature-Rich Ecosystem for Solving Differential Equations in Julia*, *Journal of Open Research Software* **5** (2017) 15.
- [48] C. Tsitouras, *Runge–Kutta pairs of order 5(4) satisfying only the first column simplifying assumption*, *Computers & Mathematics with Applications* **62** (2011) 770.
- [49] K. Bolejko and P.G. Ferreira, *Ricci focusing, shearing, and the expansion rate in an almost homogeneous Universe*, *JCAP* **05** (2012) 003.
- [50] H.J. Macpherson and A. Heinesen, *A theoretical prediction for the dipole in nearby distances using cosmography*, *The Open Journal of Astrophysics* **8** (2025) .
- [51] P. Boubel, M. Colless, K. Said and L. Staveley-Smith, *Testing anisotropic Hubble expansion*, *JCAP* **03** (2025) 066 [[2412.14607](https://arxiv.org/abs/2412.14607)].